Nature Communications

https://doi.org/10.1038/s41467-026-71158-9

Article in Press

Strain–induced spin regulation of stepped Co(111) for boosting peracetic acid magnetocatalysis

Received: 6 August 2025

Accepted: 10 March 2026

Cite this article as: Zhang, Y., Zhang, X., Qin, S. *et al.* Strain–induced spin regulation of stepped Co(111) for boosting peracetic acid magnetocatalysis. *Nat Commun* (2026). https://doi.org/10.1038/s41467-026-71158-9

Yinqiao Zhang, Xiaona Zhang, Shuhan Qin, Hao Liang, Yiming Ma, Yan Di, Wei Meng, Sijin Zuo & Minghua Zhou

Strain–Induced Spin Regulation of Stepped Co(111) for Boosting Peracetic Acid Magnetocatalysis

Yinqiao Zhang [1, 4], Xiaona Zhang [1, 4], Shuhan Qin [1], Hao Liang [1], Yiming Ma [1], Yan Di [1], Wei Meng [1], Sijin Zuo [1, 2 *] and Minghua Zhou [3]

[1] State Key Laboratory of Natural Medicines, School of Engineering, China Pharmaceutical University, Nanjing 210009, PR China

[2] Department of Chemical and Biomolecular Engineering, National University of Singapore, 117585, Singapore

[3] College of Environmental Science and Engineering, Nankai University, Tianjin 300350, PR China

[4] These authors contributed equally: Yinqiao Zhang and Xiaona Zhang

[*]Corresponding author. E–mail: sjzuo@cpu.edu.cn

Abstract

Atomic site–specific reactivity induced by the lattice distortion has garnered increasing research interest for advancing the heterogeneous catalytic conversions, owing to strain–field–tunable electronic structure of the distorted active sites. Here, we prepare the catalysts with reactive center of ferromagnetically nanoparticulate cobalt that is fully exposed by the Co(111) lattice plane with increasing strain. Such sites can boost peracetic acid (PAA) utilization under a mild magnetic field (MF, maximum 500 mT) to produce a bulk of reactive species with high ratio 93.1% R–O$^{\bullet}$ for sulfamethoxazole abatement and thus attain high–effective greener decontamination for water remediations. Spin–polarized density functional theory and experimental results collectively confirm strain–induced spin modulation at Co(111) step A sites as a critical reactivity determinant. This work integrates MF into PAA utilization and thus provides a perspective on improving the atomic economies of developing ferromagnetic nanoparticulated metal sites into water remediation in low–energy utilization route.

Introduction

In recent years highly–publicized single–atom catalysis has potently promoted the heterogeneous catalytic systems into the front research given the favorable utilization efficiency of sites [1, 2]. The catalytic sites are exclusively from one or several specific reactive activity centers including the isolated metal motif during the catalysis of wanted chemical reactions [3]. Nevertheles, still not so satisfied reaction performance that mainly resulted by the dynamic surface reconstruction of active sites into deactivation such as sites blocking via intermediates seems to be out of scope regarding our goal of cost–effective atomic economy and green, low–energy consumption [4, 5]. Cleavage of bulk sites such as metal nanoparticles to create a discontinuous surface, which will be able to produce coordinatively unsaturated atoms layout, is a relatively ideal alternative to arouse the inert bulk sites [6]. Using geometrical distortion to fabricate the discontinuous surface has been sufficiently proved to be effective for the alternative, as we reported the stretched -C–C- bond stimulating chlorination superior to the carbon defect sites [7]. Atomic–level modulation of geometrical distortion can usually achieve fine–tuning of intrinsic lattice strain of metal sites to optimize the electronic structure and energy level of reactions for enhancements of catalytic reactivity [8, 9]. For example, Jin group has reported that controllable activity of platinum by its *d*–band center depends sensitively on the lattice strain generated by an atom-doping strategy [10]. Although present research has recognized the vital role of the strain in catalytic conversions such as oxygen reduction reaction [11, 12], unveiling the underlying mechanism of strain modifying electronic state and identifying the site–specific reactivity interaction has still received insufficient attention particularly in low–cost ferromagnetic d–block metals [13]. Ferromagnetic metal-based catalytic systems combined with external magnetic field (MF) have demonstrated a competitive pathway for enhancing the atomic economy and reaction efficiency of catalytic conversions, primarily owing to the tunable chemical behavior of the intermediates to improve the interfacial mass transfer [5].

Here we use one–pot pyrolysis strategy for preparing a suit of catalysts with increasing cobalt source, termed as N–C/Co_{n-2}, CNT/Co_{n-1}, CNT/Co_n and CNT/Co_{n+1}. Characterizations including aberration–corrected high–resolution scanning transmission electron microscopy (AC–HR–STEM)

and X–ray absorption spectroscopy (XAS) unveiled the catalysts with co–existed atomically dispersed cobalt (Co SA) and ferromagnetically nanoparticulate cobalt (Co NP) decorated carbon basal planes, and the nanoparticulate cobalt displaying nearly fully exposed Co(111) facet with salient tensile strain. The catalysts were used to utilize peracetic acid (PAA) for producing reactive species toward contaminated water remediation [14, 15]. Our electron paramagnetic resonance (EPR) technology, kinetic models based on probe experiments and in–situ Raman spectroscopy all confirmed the boosted PAA utilization producing a mass of reactive species by the ferromagnetically strained Co(111) sties under the moderate MF. Spin–polarized density functional theory (DFT) and experimental results uncovered the more crucial role of strain–induced spin regulation of Co(111) particularly on step A sites in PAA activation for sulfamethoxazole (SMX) abatement [16]. Lastly, the possible detoxification pathways of SMX were deeply analyzed via DFT calculations and experiments.

Results

Characterizations of Physiochemical Structures of CNT/Co_n Series

Catalysts of CNT/Co_n composites were prepared by one–pot pyrolysis strategy at temperature 700 °C under nitrogen atmosphere (see Method for Catalysts' synthesis), in which the precursors consist of metal source of cobalt (II) nitrate hexahydrate and carbon source of dicyandiamide (Fig. S2). The catalysts with increasing cobalt are respectively termed as N–C/Co_{n-2}, CNT/Co_{n-1}, CNT/Co_n and CNT/Co_{n+1}. Aside from the well–explored role of pyrolysis temperature [17], herein we noted the vital cobalt sources in evolution of nanotube architecture by bricking carbon in situ. The cobalt sources are first converted to Co NP to catalyze growth of CNT in an interface propagation (Fig. S3). The catalyst of Co NP is easily covered by excessive carbon species leading to termination of CNT growth, when the CNT encountered not enough cobalt source. Therefore, a higher feeding of cobalt sources can be beneficial to build clearer and larger tube architectures (Figs. **1a** and b, Figs. S4 to S7). The decorated cobalt displays nanoparticles and isolated atoms, as observed by their AC–HADDF–STEM images in Fig. 1c, Figs. S8 and S9. The two readable peaks respectively pointed to Co^0 (778.7 eV of Co $2p_{3/2}$ and 794.1 eV of Co $2p_{1/2}$) and Co–N_x

bonds (781.1 eV of Co $2p_{3/2}$ and 797.2 eV of Co $2p_{1/2}$) in their X–ray photoelectron spectroscopy (XPS, Fig. S10) measurements also proves the Co–N coordination in atomically dispersed cobalt motif and the Co–Co bonds in nanoparticulate cobalt sites [18, 19]. Fourier transform (FT) k^3–weighted extended X–ray absorption fine structure (EXAFS) spectrums extracted from catalysts' Co K–edge X–ray absorption near–edge structure (XANES) and their fitting results (Fig. 1e and Figs. S11 to S13) as well as the wavelet transform plots of the catalysts (Fig. S14) unveiled a well–defined Co–N_4 motif in single–atom cobalt (Co SA) and more stretched Co–Co scattering paths in nanoparticulate cobalt when increased cobalt feeding such as 2.492 Å Co–Co path for CNT/Co_{n-1} increasing to 2.499 Å for CNT/Co_{n+1} (table S2) [19, 20]. Our molecular dynamics simulation further reveals the dynamic behavior of Co NP during the pyrolysis process (Fig. S15), showing more stretched Co–Co in Co NP with increased atomic amount.

Catalysts' X–ray diffraction (XRD) patterns display a set of notable peaks accordingly assigned to nanoparticulate cobalt with the highest intensity at ~44.2° of Co(111) facet (Fig. 1f) [19]. Rietveld refinements of the XRD data further disclose the cobalt nanoparticle having a face–centered cubic (fcc) structure with Fm–3m space group. Of note, there are the increasing lattice distances for CNT/Co_n series such as the unit cell volume from 44.38 $Å^3$ for CNT/Co_{n-1} increasing to 44.99 $Å^3$ for CNT/Co_{n+1} (table S3), showing expansion of the lattice plane [21]. It should be noted that Co(111) facets display a gradually small–angle shift (Fig. 1f enlarged). According to the Debye–Scherrer equation [7], such small–angle shift demonstrates the stretching lattice spacing toward Co(111). This shift can be also well linearly fitted in the Williamson–Hall equation (Fig. S16), and the result indicates the strain filed occurring in Co(111) [22]. The observation of increasing average lattice spacing from the intensity profiles of Co(111) planes in the inverse fast Fourier transformation patterns (Fig. 1g), such as from 0.205 nm for CNT/Co_{n-1} to 0.218 nm for CNT/Co_n, is in line with the analytical results of tensile lattice distortion in Co(111). Strain mapping of Co(111) plane based on the geometric phase analyses (GPA) from its AC–HADDF–STEM characterizations again proves the pronouncedly inhomogeneous strain fields (Fig. 1d) [23]. Wulff construction by calculating the surface energy of the low–energy facets in fcc–cobalt (Fig.

S17) corroborates that the Co(111) plane only observed in AC–HADDF–STEM images of cobalt nanoparticles (Fig. 1c and Figs. S9c, f and i) is the easiest to form due to the lowest surface energy (Fig. S17b) [24]. The pre–edge peaks in near–edge absorption energy of CNT/Co_n series from their cobalt K–edge XANES assigned to the 1s to 3d electronic transition in cobalt shows slightly bathochromic shift (Fig. 1h inset lower), indicating reduced average oxidation states and outer electrons count in the cobalt sites (Fig. S18), in good accordance with the above XPS results of cobalt (Fig. S10e) [25]. Moreover, broader peak and lower intensity for the white lines of CNT/Co_n series in their Co K–edge XANES (Fig. 1h inset upper) have been proved to occur more deformed octahedron cobalt sites. Collectively, these characterizations potently demonstrate the nearly fully exposed Co(111) facet having produced the deformed strain (Fig. 1i), and importantly, the strained sites may serve as the reactive center in subsequent reactions since cobalt is the most active among all elements in the catalysts (Fig. S19).

CNT/Co_n Series Activating PAA for Generating Reactive Species

The catalysts are used to utilize a green and well–received bactericide, peracetic acid (PAA, Fig. S20), since PAA can produce long–life, highly selective reactive species, such as carbon–centred radical (R–O$^{\bullet}$, Fig. S21 and table S4), after being activated [26]. Our experimental results showed that PAA utilizations are substantially boosted by the strained Co(111) (Fig. **2a**), and the optimum performance is attained by CNT/Co_n with the highest k_{PAA} of 0.16 min^{-1} (a descriptor for PAA utilization, Fig. S22). Negligible performance in PAA utilization from the catalysts (N/C) prepared without cobalt source underscores the important role of cobalt sites. As there are similar amounts and motifs for Co SA in CNT/Co_n series (Fig. 1e and Fig. S10e and table S2) and even the nearly same ratio of defects versus graphitization for carbon basal plane (Fig. S23), we reason that the boosted performance may be related to the nanoparticulate cobalt sites particularly in the nearly fully exposed Co(111) facet with strain field. First–principle DFT calculation indicates that the spin charge density around at Co SA is substantially remodeled by Co(111) (Fig. S24), and a more energetically favorable adsorption in 3O of PAA molecule was observed for -0.51 eV of Co(111) higher than -0.21 eV of Co SA (Figs. S25 and S26). Convincingly, a counterpart of

CNT/Co_{SA} that was obtained by the intensively acid leaching of CNT/Co_n to remove the nanoparticulate cobalt displaying inert reactivity for PAA activation (Figs. S27 and S28) [17], also underlines the importance role of strained Co(111) in our systems.

Reactive species generated from the above catalytic process were first detected by EPR technology using the spin trapper of 5,5–dimethyl–l–pyrroline N–oxide (DMPO). The obvious sevenfold peak assigned to 5,5–dimethyl–2–pyrrolidone–*N*–oxyl (DMPOX) product (Fig. 2b) verifies generation of strongly oxidative species after PAA activation, and the species might be the R–O$^{\bullet}$ [27, 28]. Kinetic models based on probe experiments further detail the types and exposures of reactive species in present systems (Fig. S29) [29]. The results showed that CNT/Co_n/PAA system has almost achieved 3–fold free radical exposure greater than CNT/Co_{n-1}/PAA, and a high 87.5% ratio of R–O$^{\bullet}$, as shown in Fig. 2c. Mass spectrometry analysis for identifying R–O$^{\bullet}$ by a classic trapper of 2,2,6,6–tetramethyl–1–piperidinyloxy (TEMPO) showed the identifiable $CH_3C(O)O$–TEMPO signal at m/z 215.2 and absent signals of methyl ($^{\bullet}CH_3$) and acetylperoxyl radical ($CH_3C(O)OO^{\bullet}$) (Fig. S30), and $^{\bullet}CH_3$ was also excluded by the dissolved oxygen–associated experiment (Fig. S31) [30, 31]. These results disclose $CH_3C(O)O^{\bullet}$ as main reactive species among R–O$^{\bullet}$ in our system. It may be related to high instability for $CH_3C(O)OO^{\bullet}$ and secondary radical for $^{\bullet}CH_3$ from $CH_3C(O)OO^{\bullet}$ [30]. Hence, these experimental results have impressed the strain field not only enhancing PAA utilization but tuning the types of reactive species in our system. Characterizations of in–situ Raman spectroscopy further reveal accelerating PAA consumption occurred on CNT/Co_n compared that of CNT/Co_{n-1} at rough 630 cm^{-1} stretching, and vitally, a slightly bathochromic from 552 cm^{-1} for CNT/Co_n to 535 cm^{-1} for CNT/Co_{n-1} indicates the intensive charge interaction between PAA and CNT/Co_n (Fig. 2d) [32]. An illustrative demonstration is that the amperometric curves displaying more excited currents after PAA addition for our catalysts particular for CNT/Co_n (Fig. S32a), not only highlighted direct utilization of the bactericide by our catalysts without so–called third–party mediators, such as electron donor of organics [33], but pointed out the key for the intensive charge interaction that is attributed to the favorable electron transfer between PAA and the strained Co(111) sites. This can be explained by

the strained sites having the active electron transfer ability, such as easier electron exchange and lower interface resistance for CNT/Co_n that are respectively supported from a suit of higher catalytic waves (Fig. S33a) and smaller transfer impedance (Fig. S33b) in their electrochemical tests [34].

Mechanism Investigation in PAA Utilization by CNT/Co_n Series

We try to elucidate the mechanisms behind enhanced active electronic behaviors occurring on the strained Co(111) sites. We reexamined the cobalt XPS spectra (Fig. S34), and observed the similar redshift of the binding energy of two main peaks at Co $2p_{3/2}$ and $2p_{1/2}$, again revealing the formed strain fields [10]. Importantly, the gradually augmented energy differences (ΔE) between the binding energies of two main peaks that are caused by spin–orbital splitting implies the increasing number of unpaired electrons [35]. The unpaired electrons of cobalt sites can be conventionally depicted by the effective magnetic moments (μ_{eff}), and the μ_{eff} was further calculated by the Curie–Weiss law according to their temperature–related magnetic susceptibility (Fig. S35). The result revels the *d* electronic states in CNT/Co_n being 0.79 of high–spin and 0.21 of low–spin polarization as well as the highest μ_{eff} (the largest Curie constant) shown in Fig. **3a**. Notably, both μ_{eff} and ratio of high–spin electrons well matched with the k_{PAA} value of PAA utilization toward CNT/Co_n series (Fig. 2e). These results highlight the crucial role of high–spin electrons in CNT/Co_n for PAA utilization. We thus reason that the strain fields have caused spin splitting in the partially occupied *d*–state electrons [36].

The electronic structure of cobalt sites was further simulated and analyzed by the density of states (DOS) in the model of Co(111)/Co SA based on spin–polarized DFT calculation. The calculation results show that the contributions of Co SA to total DOS are very inappreciable (Figs. S36 and S37), and again underline the vital role of Co(111) in contributing to activity. We thus focused on the electronic state using the model of Co(111) in subsequent discussion. As shown in Fig. 3b, because of the octahedron crystal field in our Co(111) sites, *d* states will be divided into e_g (d_{z2} and d_{x2-y2}) and t_{2g} (d_{xy}, d_{xz} and d_{yz}) with orbital splitting energy of 2.62 eV [37]. The strain field reduce the electronic spin–flipping barriers to improve spin polarization that comes from the

unpaired occupied stated electrons, in light of the strong delocalization loss of *d* electrons in Co(111) sites [38]. The crystal filed energy splitting thus decreased to 1.40 eV and reduced level degeneracy occurred. After 7% strain in Co(111), minutely, the energy level of e_g and t_{2g} both decreased especially for e_g from 1.89 eV of unoccupied state dropping to -0.11 eV of occupied state (Figs. 3b and c). This leads to the elevated spin polarization of e_g particularly for contributions of the d_{x2-y2} orbital, and the improved net spin electronic states (Δd) from 2.23 to 2.60 |e|. Accordingly, the spin magnetic moment increased from 1.77 μB for the unstrained Co(111) to near 1.84 μB for the 7%–strained (Fig. 3d), agreeing well with the foregoing experimental results of zero–filed cooling tests. The increasing spin magnetic moment reduces the work functions from 5.062 eV to 4.882 eV and enables the *d*–band center to near the Fermi level (Fig. 3d and Figs. S38 to S41). These energy variations have presumably caused a volcano-type relationship between the cobalt site and peroxy bond (Fig. S42), and thus soundly explained the boosting catalytic performance of PAA utilization toward CNT/Co_n.

An abundance of electrons in occupied state below the Fermi level for e_g orbitals have been evidenced from the coordinatively unsaturated cobalt sites in Co(111) especially for stepped edges [39]. Here Co(111) sites make up of middle terrace sites and two–side step sites (step A and step B) as illustrated in Fig. S43 [24]. The sites have atomic–resolved strain fields and variable electronic spin exchanging ability such as the highest magnetic moments of 1.96 μB occurring in 7%–strained step A sites (Fig. S43f) [40]. This highlights step A sites not only have more energetically favorable chemosorption of PAA (PAA*) with a benign value of -0.53 eV, but also display an exothermal energy transfer with a value of -0.55 eV during the crucial process of PAA cleavage, as shown in Fig. 3g and Fig. S44. Contrastively, both step B and terrace sites display the endothermal energy variations toward PAA activation, such as +0.35 eV energy barrier being expended for the terrace sites. As a result, we can clearly observe more significant charge accumulation and depletion on the 1Co–3O bridge between step A and PAA molecule in their charge density difference calculation, as demonstrated in Fig. 3e and Fig. S45. For example, Bader charge of step A would loss 0.18 |e| to PAA in 1Co–3O stretching while only 0.15 |e| and 0.12 |e|

transfer respectively occur in terrace and step B sites. The spin exchange interactions of the darting electron in 1Co–3O stretching further unveil the similar shuttling patterns of unpaired electron for the three sites but the most active intensity from step A (Fig. 3f). Overall, we can conclude that the step A sites of Co(111) make the greatest contribution to PAA activation.

Boosting PAA utilization via magnetocatalysis of CNT/Co_n

We observed the high–spin global room–temperature ferromagnetism in CNT/Co_n by its magnetization curve (Fig. S46). The linewidth of the EPR plots of CNT/Co_n, taken from the peak–to–peak distance (ΔE), decreased with increasing the temperature from 100 to 300 K, which indicate CNT/Co_n's ferromagnetic order behaviors (Fig. 2f) [5]. Given the cobalt's bifunctional nature of spin effects and ferromagnetic behavior here, we tentatively used a commonly available magnetic field (MF, maximum 500 mT) to assist PAA utilization. As expected, CNT/Co_n ferromagnetic catalysis for PAA utilization was boosted roughly 1.3 times higher than without external MF (Fig. 2g). Awaked current signal under increasing MF intensity after adding PAA and even SMX can be observed from a current–MF map of CNT/Co_n in Fig. 2h. The current signal was further magnified with increasing multi–potential steps under ranging from 0.8 to 1.1 V, and returned to its original value after a periodic potential applied, implying the robust structure of CNT/Co_n (Fig. 2i). All these experimental results clearly underpin the superiority of CNT/Co_n in PAA utilization by combining an external MF. It is due to the certified fact that the short–range quantum spin exchange assisted by long–range room–temperature ferromagnetic ordering enables providing effectively spin–cleavage means to accelerate intermediates' desorption dynamics [24, 41], in light of the desorption kinetics of intermediates as an unfriendly rate–controlling step during PAA activation (Fig. 3g). Resultantly, exposure of reactive species generated by MF–assisted CNT/Co_n/PAA system has a 1.9–folds increase than that without MF (Fig. S47 and Fig. 2c). However, the distribution and type of the reactive species are nearly not changed, such as the almost stable R–$O^{\bullet}$ ratio of 93.1% under MF versus 87.5% without MF, since our experimental results from characterization of active sites unveil that MF does not hatch newborn active sites in the catalyst for PAA magnetocatalysis (Figs. S48 and S49).

CNT/Co_n/PAA system for water decontamination

In view of the above remarkable performance of PAA utilization by CNT/Co_n magnetocatalysis, the bactericide was used in contaminated water remediation as the surging demand for clear water resources [42, 43]. We chose sulfamethoxazole (SMX, Fig. S50) as a model contaminant for evaluating the performance of the above systems given sulfa as the widely detected pharmaceutical contaminants in the water environment [16]. After optimized dosage of reactants (Fig. S51), CNT/Co_n/PAA system toward SMX abatement demonstrates a brilliant performance among the presently most popular oxidants such as persulfate or hydrogen peroxide (Figs. S52 and S53) and other works (Fig. S54 and tables S6 and S7). It also displays pH 6–9 adaptation and immunity to some common water background factors (Figs. S55 and S56), such as humic acid (a common natural organic matter in water environment), chlorine ion and even bicarbonate ion. A set of scavengers including methanol, 2,4–hexadiene, β–carotene and TEMPO, inhibiting SMX abatement as anticipated (Fig. S57) again underline the main contributor of R–$O^{\bullet}$ and no other promotors such as adsorption (Fig. S58) and current routinely detected reactive species including superoxide radical (Fig. S59), singlet oxygen (Fig. S60) or high–valence cobalt species (Fig. S61) in CNT/Co_n/PAA system [7, 36].

CNT/Co_n series activating PAA for SMX abatement after applying MF (Fig. **4a** and Fig. S62) appears similar activity trends with PAA utilizations without MF (Fig. 2a), that is, CNT/Co_n shows the best performance, albeit high decoration densities of cobalt would occur in coupling from localized magnetic moment under MF (Figs. S7 and S46) [41]. The phenomenon highlights the crucial role for strain–induced spin regulation of the stepped Co(111) in PAA utilization (Fig. S63 and Fig. 4c). Interestingly, MF–boosted SMX removal in our CNT/Co_n/PAA system while underactivity in CNT/Co_{SA}/PAA system can be directly observed (Fig. 4b and Fig. S46). These results seem to declare a greater strength for the ferromagnetic strained Co(111) than the highly–publicized single cobalt atom catalysis. We further constructed a continuous–flow reactor for evaluation the possible real application of our system (Fig 4d and Fig. S64) [7]. As a key component of the reactor, the home–made CNT/Co_n membrane displayed undamaged nanotube

architecture (Fig. 4e) and roughly 160 μm thickness (Fig. 4f). This reactor displays effective treatments regarding SMX, tetracycline and methylene blue with more than 98% degradation rate lasting up to 600 min (Fig. 4g). The steady performance again demonstrates the robust physicochemical structure of CNT/Co_n catalyst and MF is likely conducive to refreshing the active sites (Figs. S65 to S67 and table S8).

We analyzed the possible products and degradation pathways during the SMX abatement. The results presented six main intermediates via mass spectrometry characterizations (Fig. S68). We thus reckoned three degradation pathways of SMX in our system (Figs. S69 and S70), mainly involving hydroxylation (pathway I), cleavage of sulfonamide bond (pathway II) and polymerization (pathway III). In pathway I (Fig. 4h and Fig. S71), the amino group in SMX would first form a nitrogen–centred radical (•NH–R1) via hydrogen atom abstract by radical attacking of $CH_3C(O)O^{\bullet}$ or $^{\bullet}OH$ due to the highest f^0 on 23N (Fig. S50 and table S5) and then hydroxylation occur via the free–radical addition to produce P2. In pathway II, based on the thermodynamical calculations (Fig. 4i and Fig. S72a), the pivotal heterolytic cleavage of sulfonamide bond (26S–11N) was only conducted by electrophilic attacking of $CH_3C(O)O^{\bullet}$ to form the precursors of P3 (R_2-$O_2S^{+}_{\bullet}$) and P5 ($^{-}$NH–R_3). It may be related to the high electrophilicity of 26S (0.11 eV, table S5) and the highest electronic affinity of $CH_3C(O)O^{\bullet}$ (6.10 eV, table S4) [44]. Free–radical addition of the precursors of P3 and P5 would severally occur (Fig. S72b) and the spontaneous acid–based pair (Fig. S72c) to generate P3 and P5. In pathway III, a free-radical-triggered single electron transfer generates nitrogen–centred radicals ($\dot{N}$-R_1 and $\dot{N}$-R_3) from SMX and product P5. These radicals then couple to yield the polymer P1, a thermodynamically favorable reaction (ΔG = -77.63 kcal/mol, Fig. 4j and Fig. S73c). As such, SMX was abated into greener small molecular products (Fig. S74) in $CH_3C(O)O^{\bullet}$–dominated and $^{\bullet}OH$–involved detoxification pathways, which well aligns with the foregoing conclusions of Figs. 2b and c.

Discussion

We reported a strain–induced spin regulation on Co(111) sites for boosting PAA

magnetocatalysis into contaminated water remediation. The cobalt precursors have a vital impact on tuning the lattice distance to create the tensile strain of Co(111). The strain field has regulated the *d*–state electronic structure to form higher local magnetic moment, and reduced the spin–flipping energy to produce more spin–polarized unpaired electrons. With such exciting high–spin electronic state in the active sites particular for step A of Co(111), it thus displayed high–effective PAA magnetocatalysis to generate a bulk of reactive species with high ratio 93.1% R–O$^{\bullet}$ for greener detoxification of SMX in water remediation.

Even though we have fulfilled encouraging bench–scale results including deep mechanical insight of the strain inducing spin regulation and long–effective water remediation, the under–discussed promotion mechanisms by MF and generalized catalyst design principle would have a prospect toward traditionally underutilized magnetic materials (such as cobalt and nickel, Fig. S75) for the bactericide utilization, maximizing the atom economies and energy efficiencies in near industrialization [45].

Methods

Chemicals and Reagents. All reagents were at least analytical grade and used as received without further purification. Sulfamethoxazole (SMX), naproxen, and 2,2,6,6–tetramethylpiperidin–1–oxy radical (TEMPO) were purchased from Sigma–Aldrich Co., Ltd. (St. Louis, MO, USA). Cobalt nitrate hexahydrate ($Co(NO_3)_2$•$6H_2O$), dicyandiamide ($C_2H_4N_4$), methyl alcohol (MeOH), furfuryl alcohol (FFA), L–histidine, β–carotene, 2,4–hexadiene (2,4–HD), sodium thiosulfate ($Na_2S_2O_3$), terephthalic acid, 9,10–diphenylanthracene (DPA), methyl phenyl sulfoxide (PMSO), methyl phenyl sulfone ($PMSO_2$), sodium bicarbonate ($NaHCO_3$), sodium chloride (NaCl), sodium sulphate (Na_2SO_4), sodium hydroxide (NaOH), sulfuric acid (H_2SO_4), potassium iodide (KI), humic acid (HA), methylene blue, ethylenediamine tetraacetic acid disodium salt (EDTA–2Na), sodium hypochlorite, sodium perborate ($NaBO_3$), potassium peroxodisulfate, potassium peroxymonosulfonic acid ($H_3K_5O_{18}S_4$), hydrogen peroxide (H_2O_2), N,N–dimethylformamide were obtained from Aladdin Biological Technology Co., Ltd. (Shanghai, China). Acetonitrile (ACN) of high–performance liquid chromatography (HPLC) grade was

purchased from Anhui Tiandi Life Science and Technology Co., Ltd. Except for DPA stock solution, which was prepared using ACN as the solvent, all the stock solutions were prepared in Milli–Q water (>18.2 MΩ·cm).

Characterizations. The physical morphologies of catalysts were characterized by Transmission Electron Microscopy (TEM), high–resolution TEM (HRTEM, JEM–2100 HR, JEOL) and aberration–corrected high–angle annular dark–field scanning transmission electron microscopy (AC–HAADF–STEM, JEM–ARM300F2, JEOL) equipped with a Gatan image filter spectrometer. Geometric phase analysis (GPA) to characterize the strain distribution of catalysts was obtained by an open–source program Strain^{++} plug in the software of Digital Micrography. Raman spectra were recorded on the Raman spectrometer (LABRAM HR800) under the excitation of a 532 nm laser. The surface element valence states of catalysts were examined with K–Alpha X–ray Photoelectron Spectrometer (XPS). X–ray diffraction (XRD, Bruker–D8 Instrument) using Cu Kα radiation (λ 0.15418 nm) was used to analyze the crystalline structure of catalysts. Concentrations of organics were determined by the high–performance liquid chromatography (HPLC, LC–20AT, Shimadzu, Japan) equipped with a Waters C18 analytical column (4.6 mm×150 mm, particle size 5 μm) and a diode array detector (DAD). Intermediates of SMX degradation were detected by liquid chromatography–mass spectrometry (LC/MS, Agilent 1260/6420). Concentration of cobalt ion was measured by inductively coupled plasma mass spectrometry technique (ICP-MS, Perkin Elmer Nexion 100). Electron paramagnetic resonance (EPR, EMX–10/12, Bruker) technology was adopted to analyze the physicochemical structure of catalysts and the reactive species generated in reaction systems. Zero field cooled measurements were carried out by magnetic property measurement system (SQUID–VSM, Quantum Design) under 1 kOe. The X–ray absorption experiments were carried out at the XAFS station (BL14W1) at the Shanghai Synchrotron Radiation Facility (SSRF), China. Co foil, CoO, Co_2O_3 and cobalt phthalocyanine (CoPc) were used as reference samples. The magnetism measurements were conducted in a commercial magnetic property measurement system (MPMS–squid VSM–094).

Catalysts' synthesis. 2.9 g DCD and 1.0 g $Co(NO_3)_2$•$6H_2O$ were put into a 2 mL ethanol

solution. The foregoing mixtures were placed in an agate mortar and continuously grinded until forming uniform pink pastes. Then, the pastes were annealed at 700 °C for 3.5 hours with a ramping rate of 5 °C min^{-1} under a nitrogen atmosphere to obtain the powder catalyst termed as CNT/Co_n. Acid wash of the obtained catalysts to remove some impurities such as weakly–bonded cobalt debris was conducted in 0.5 M H_2SO_4 for 4 hours. The catalysts of N/C, N–C/Co_{n-2}, CNT/Co_{n-1} and CNT/Co_{n+1} were respectively prepared by adjusting the dosage of $Co(NO_3)_2$•$6H_2O$ to 0, 0.1, 0.5, and 2.0 g.

PAA utilization. During PAA activation process, 200 μM PAA was added into 200 mL reaction solution without target contaminant addition, and subsequently 10 mg L^{-1} catalyst was added for utilizing PAA to produce reactive species. To detect PAA activation under the magnetic field (MF), a magnet (60×40×10 mm) was introduced as an applied magnetic field and placed on the side wall of a beaker containing 200 mL of PAA solution. MF strength was adjusted by setting different numbers of magnets and measured by Gaussmeter magnetic tester (TD8620, Changsha Tianheng Measurement and Control Technology Co., Ltd.). In PAA magnetocatalysis process, the dosage of catalysts was improved to 100 mg L^{-1} to strengthen magnetism response of the reaction systems, and accordingly, the usage of PAA decreased to 120 μM. The utilization efficiency of PAA was quantified by the *k* value obtained from the pseudo–first–order kinetic model as equation (1) shown below.

$$-\ln\frac{C}{C_0}=kt \qquad (1)$$

Contaminant abatement. During contaminant degradation by PAA activation process, taken SMX as example, 2.5 mg L^{-1} SMX and PAA were simultaneously added into 200 mL reaction solution containing pre–dosed catalyst. At predetermined intervals, 1.0 mL reaction solution and 1.0 mL $Na_2S_2O_3$ solution (1.6 g L^{-1}) were mixed immediately to stop catalytic reaction. The above filtered solution was used to analyze the concentration of SMX by an HPLC system. The mobile phase was acetonitrile versus water (55:45, v/v%) with a flow rate of 1.0 mL min^{-1}, and the detection wavelength was selected at 265 nm.

Electrochemical experiments. Electrochemical experiments were performed using a CHI 760E electrochemical workstation equipped with standard three–electrode electrochemical cells in 50 mM Na_2SO_4 solution, where counter electrode of platinum wire, reference electrode of saturated calomel electrode (SCE) and work electrode of carbon paper (1×2 cm) covered with the testing catalysts were applied. The catalyst ink was prepared by mixing 1 mg catalyst, 950 μL ethanol solution and 50 μL Nafion by sonication for 1 hour. The prepared catalyst ink was uniformly sprayed onto the carbon paper for severing as a working electrode.

DFT calculation. The density of states (DOS), work function, Fermi level, and adsorption energy etc., were calculated by the density functional theory (DFT) calculations using the Vienna Ab initio Simulation Package (VASP) within the generalized gradient approximation (GGA) using the Perdew–Burke–Ernzerhof (PBE) functional. The projected augmented wave (PAW) potentials were chosen to describe the ionic cores. The cutoff energy of 450 eV for planewave basis set was used. A 20 Å vacuum space was applied along the Z–direction to reduce the mirror image interaction. The Brillouin zone was sampled with 3×3×1 Monkhorst–Pack k–mesh. Geometry optimizations were performed with the force convergency smaller than 0.02 eV/Å. Grimme's DFT–D3 method was applied to the dispersion correction. The vacuum thickness was set 20 Å. The model of cobalt single atom (Co SA) contained 39 atoms. The model of Co (111) contained 3 layers of Co atoms (60 atoms).

To investigate the most likely exposed crystal plane for fcc–Co surfaces, we built a Wulff construction by calculating the surface energy of each crystal plane [24]. The slabs of each crystal plane have 8 layers of cobalt atoms and a 20 Å vacuum space was applied along the z–direction. The Brillouin zone was sampled with 12×12×1 Monkhorst–Pack k–mesh. The surface energy ($E_{surface}$) can be calculated according to equation (2).

$$E_{surface} = (E_{total} – N \times E_{bulk})/2A \quad (2)$$

where, N is the number of atoms in the slab; E_{total} is the calculated total energy of the slab; E_{bulk} is the total energy per atom of fcc–Co, and A is the surface area of the slab.

Calculation for the effective magnetic moment of catalysts. The effective magnetic

moment (μ_{eff}) can be calculated according to equations (3–4) [46].

$$\mu_{eff} = \sqrt{8C}\mu_B \quad (3)$$

$$\mu_{eff} = \sqrt{n(n+2)}\mu_B \quad (4)$$

where, μ_B is Bohr magneton, C is Curie constant, n is the number of single electrons.

C is derived from a linear fitting of χ^{-1}–T curve based on the Curie−Weiss law as shown in equation (5).

$$\chi = \frac{C}{T - \theta} + \chi_0 \quad (5)$$

where, χ is susceptibility, χ_0 is a constant susceptibility independent of temperature. θ and T are Curie−Weiss temperature and experimental temperature, respectively.

After the μ_{eff} is obtained, the fractions of low– and high–spin states (V_{LS} and V_{HS}) can be calculated according to equations (6–7) [47].

$$\mu_{eff} = g\mu_B \sqrt{S_{LS}(S_{LS}+1)V_{LS} + S_{HS}(S_{HS}+1)V_{HS}} \quad (6)$$

$$V_{LS} + V_{HS} = 1 \quad (7)$$

where, g is the Lande g−factor (g=2 for electron), S_{LS} and S_{HS} are total spin angular momentum of low and high spin states, respectively.

Data Availability

All the raw data relevant to the study are available from the corresponding author upon request. Source data are provided with this paper.

References

[1] G. D. Liu, A. J. Shih, H. Q. Deng, K. Ojha, X. T. Chen, M. C. Luo, I. T. Mccrum, M. T. M. Koper, J. Greeley, Z. H. Zeng, Site-specific reactivity of stepped Pt surfaces driven by stress release, Nature, 2024, **626**, 1005-1001.

[2] Z. Chen, J. Y. Wang, B. Yang, J. Li, Z. Y. Liang, X. Y. Liu, Y. Bao, J. Z. Cao, M. Y. Xing, Organic carbon transfer process in advanced oxidation systems for water clean-up, Nat. Water, 2025, **3**, 334-344.

[3] T. Y. Zhao, J. J. Wang, Y. R. Wei, Z. C. Zhuang, Y. H. Dou, J. R. Yang, W. H. Li, D. S. Wang, From lab-scale to industrialization: atomically M-N-C catalysts for the oxygen reduction reaction, Energ. Environ. Sci. 2025, **18**, 3462-3501.

[4] H. H. Zhao, X. Xu, W. Q. Cui, L. L. Geng, X. M. Peng, J. R. Yang, X. Z. Shao, Y. B. Liu, Synchronization strategy for activity and stability in Fenton-like single-atom catalysis, Adv. Mater. 2025, 2503217.

[5] T. Sun, Z. Y. Tang, W. J. Zang, Z. J. Li, J. Li, Z. H. Li, L. Cao, J. S. D. Rodriguez, C. O. M. Mariano, H. M. Xu, P. Lyu, X. Hai, H. H. Lin, X. Y. Sheng, J. W. Shi, Y. Zheng, Y. R. Lu, Q. He, J. S. Chen, K. S. Novoselov, C. H. Chuang, S. B. Xi, X. Luo, J. Lu, Ferromagnetic single-atom spin catalyst for boosting water splitting, Nat. Nanotechnol. 2023, **18**, 763-771.

[6] L. Wang, Z. H. Zeng, W. P. Gao, T. Maxson, D. Raciti, M. Giroux, X. Q. Pan, C. Wang, J. Greeley, Tunable intrinsic strain in two-dimensional transition metal electrocatalysts, Science, 2019, **363**, 870-874.

[7] Y. Q. Zhang, M. H. Chen, X. Y. He, E. Z. Zhao, H. Liang, J. G. Shang, K. Liu, J. Q. Chen, S. J. Zuo, M. H. Zhou, Intrinsic strain of defect sites steering chlorination reaction for water purification, Nat. Commun. 2025, **16**, 2652.

[8] L. K. Zheng, M. Y. Wei, F. T. Eickemeyer, J. Gao, B. Huang, U. Gunes, P. Schouwink, D. W. Bi, V. Carnevali, M. Mensi, F. Biasoni, Y. X. Zhang, L. Agosta, V. Slama, N. Lempesis, M. A. Hope, S. M. Zakeeruddin, L. Emsley, U. Rothlisberger, L. Pfeifer, Y. M. Xuan, M. Grätzel, Strain-induced rubidium incorporation into wide-bandgap perovskites reduces photovoltage loss, Science, 2025, **388** ,88-95.

[9] J. Chen, C. Liu, S. Xi, S. Tan, Q. He, L. Liang, X. Liu, Optical nonlinearities in excess of 500 through sublattice reconstruction, Nature, 2025, **643**, 669–674.

[10] T. O. He, W. C. Wang, F. L. Shi, X. L. Yang, X. Li, J. B. Wu, Y. D. Yin, M. S. Jin, Mastering the surface strain of platinum catalysts for efficient electrocatalysis, Nature, 2021, **598**, 76-81.

[11] R. Zeng, H. Q. Li, Z. X. Shi, L. Xu, J. H. Meng, W. X. Xu, H. S. Wang, Q. H. Li, C. J. Pollock, T. Q. Lian, M. Mavrikakis, D. A. Muller, H. D. Abruña, Origins of enhanced oxygen reduction activity of transition metal nitrides, Nat. Mater. 2024, **23**, 1695-1703.

[12] R. M. Kluge, R. W. Haid, A. Riss, Y. Bao, K. Seufert, T. O. Schmidt, S. A. Watzele, J. Barth, F. Allegretti, W. Auwärter, F. Calle-Vallejo, A. S. Bandarenka, A trade-off between ligand and strain effects optimizes the oxygen reduction activity of Pt alloys, Energ. Environ. Sci. 2022, **15**, 5181-5191.

[13] T. Z. Wu, X. Ren, Y. M. Sun, S. N. Sun, G. Y. Xian, G. G. Scherer, A. C. Fisher, D. Mandler, J. W. Ager, A. Grimaud, J. L. Wang, C. M. Shen, H. T. Yang, J. Gracia, H. J. Gao, Z. C. J. Xu, Spin pinning effect to reconstructed oxyhydroxide layer on ferromagnetic oxides for enhanced water oxidation, Nat. Commun. 2021, **12**, 3634.

[14] Y. Chen, Q. Li, R. Su, Y. Gao, N. An, Y. Rong, X. Xu, D. Ma, Y. Wang, B. Gao, Oxygen vacancies-mediated the peracetic acid activation to selectively generate $^1O_2$ for water decontamination, Water Res. 2025, **282**, 123765.

[15] S. Li, J. Zou, J. Y. Wu, L. F. He, C. Y. Tang, F. Li, B. Sun, M. Zhao, Q. S. Li, P. P. Wang, L. S. Huang, Q. F. Cheng, H. Q. Tan, J. Ma, Removal of sulfonamide antibiotics in peracetic acid-mediated natural polyphenol systems via an overlooked polymerization pathway: role of ortho-quinones, Environ. Sci. Technol. 2025, **59**, 7747-7759.

[16] S. Baumgartner, M. Salvisberg, P. Schmidhalter, T. R. Julian, C. Ort, H. Singer, Insights into respiratory illness at the population level through parallel analysis of pharmaceutical and viral markers in wastewater, Nat. Water, 2025, **3**, 580-589.

[17] J. Kang, L. Zhou, X. G. Duan, H. Q. Sun, Z. M. Ao, S. B. Wang, Degradation of cosmetic microplastics via functionalized carbon nanosprings, Matter, 2019, **1**, 745-758.

[18] R. D. Su, Z. Liu, J. S. Qiu, N. Li, X. Xu, B. Y. Gao, Q. Li, Photoexcited hole-enabled synthesis of surface high-valent cobalt-oxo species with water as the oxygen atom source for water purification, Angew. Chem. Int. Ed. 2025, e202507085.

[19] X. Y. Cheng, J. Yang, W. Yan, Y. Han, X. M. Qu, S. H. Yin, C. Chen, R. Y. Ji, Y. R. Li, G. Li, G. Li, Y. X. Jiang, S. G. Sun, Nano-geometric deformation and synergistic Co nanoparticles-Co-N composite sites for proton exchange membrane fuel cells, Energ. Environ. Sci, 2021,**14**, 5958-5967.

[20] X. Guo, H. Zhang, Y. Wang, Y. Yao, C. Xiao, K. Gu, J. Qi, Y. Zhou, Y. Yang, Z. Zhu, J. Li, Confining asymmetrically coordinated cobalt single-atoms/clusters on holey Mxene for ultrafast Fenton-like catalysis, Angew. Chem. Int. Ed. 2025, e202511266.

[21] B. X. Ge, P. Y. Jiang, B. Y. Chen, C. J. Huang, Controlling Co 3d/O 2p orbital hybridization in $LaCoO_3$ by modulating the Co-O-Co bond angle for enhanced oxygen evolution reaction catalysis, ACS Catal. 2025, **15**, 477-486.

[22] C. H. Chen, Q. H. Zhou, Z. Y. Guo, H. Li, C. Miao, D. Chen, X. H. Hu, X. Feng, V. Noël, S. Ghoshal, G. V. Lowry, L. Z. Zhu, D. H. Lin, J. Xu, Lattice-sulfur-impregnated zero-valent iron crystals for long-term metal encapsulation, Nat. Sustain. 2024, **7**, 1264-1272.

[23] S. Maiti, K. Maiti, M. T. Curnan, K. Kim, K. J. Noh, J. W. Han, Engineering electrocatalyst nanosurfaces to enrich the activity by inducing lattice strain, Energ. Environ. Sci. 2021, **14**, 3717-3756.

[24] K. Zhang, A. Cao, L. H. Wandall, J. Vernieres, J. Kibsgaard, J. K. Norskov, I. Chorkendorff, Spin-mediated promotion of Co catalysts for ammonia synthesis, Science, 2024, **383**, 1357-1363.

[25] X. Zhang, H. Y. Zhong, Q. Zhang, Q. H. Zhang, C. Wu, J. C. Yu, Y. F. Ma, H. An, H. Wang, Y. M. Zou, C. Z. Diao, J. S. Chen, Z. G. Yu, S. B. Xi, X. P. Wang, J. M. Xue, High-spin Co^{3+} in cobalt oxyhydroxide for efficient water oxidation, Nat. Commun. 2024, **15**, 1383.

[26] J. H. Wu, T. H. Yang, Y. J. Sun, Y. Min, Y. Hu, F. Chen, J. J. Chen, H. Q. Yu, Tailoring the selective generation of oxidative organic radicals for toxic-by-product-free water decontamination, Proc. Natl. Acad. Sci. U. S. A. 2024, **121**, e2403544121.

[27] S. Li, Y. L. Yang, J. F. Niu, H. S. Zheng, W. Zhang, Y. K. Leong, J. S. Chang, B. Lai, Activation of PAA at the Fe-N_x sites by boron nitride quantum dots enhanced charge transfer generates high-valent metal-oxo species for antibiotics degradation, Environ. Sci. Technol. 2024, **58**, 21871-21881.

[28] L. Chen, R. Zhang, Z. Liu, F. Li, B. Huang, W. Liu, Accurate identification and formation mechanism unraveling of radicals in UV-induced peracetic acid activation system using in-situ electron paramagnetic resonance, Sci. Bull. 2025, **70**, 1581-1585.

[29] S. Zuo, R. Guo, W. Xue, J. Shang, J. Chen, Y. Zhang, Decipher the key role of ketone toward

singlet oxygen evolution in Fenton-like process for water decontamination, Appl. Catal. B Environ. 2023, **339**, 123100.

[30] J. Y. Wu, J. Zou, J. B. Lin, S. Li, L. F. He, Z. J. Wu, Q. S. Li, C. M. Gong, J. Ma, Overlooked role of coexistent hydrogen peroxide in activated peracetic acid by Cu(II) for enhanced oxidation of organic contaminants, Environ. Sci. Technol. 2024, **58**, 15741-15754.

[31] L. Meng, J. Y. Dong, J. Chen, L. Li, Q. G. Huang, J. H. Lu, Activation of peracetic acid by spinel $FeCo_2O_4$ nanoparticles for the degradation of sulfamethoxazole, Chem. Eng. J. 2023, **456**, 141084.

[32] M. Y. Lan, Y. H. Li, C. C. Wang, X. J. Li, J. Z. Cao, L. H. Meng, S. Gao, Y. H. Ma, H. D. Ji, M. Y. Xing, Multi-channel electron transfer induced by polyvanadate in metal-organic framework for boosted peroxymonosulfate activation, Nat. Commun. 2024, **15**, 7208.

[33] J. Shi, Y. Cheng, T. Wang, Y. Peng, X. Lin, B. Tang, M. Feng, Z. Zhuang, Y. Sun, X. Yu, Z. J. Xu, Site-specific spin state modulation in spinel oxides for enhanced nonradical oxidation, Angew. Chem. Int. Ed. 2025, e202504189.

[34] H. Xu, M. W. Wang, S. Q. Hei, X. Qi, X. Y. Zhang, P. Liang, W. Y. Fu, B. C. Pan, X. Huang, Neglected role of iron redox cycle in direct interspecies electron transfer in anaerobic methanogenesis: Inspired from biogeochemical processes, Water Res. 2024, **262**, 122125.

[35] K. Sun, Y. Huang, Q. Y. Wang, W. D. Zhao, X. S. Zheng, J. Jiang, H. L. Jiang, Manipulating the spin state of Co sites in metal-organic frameworks for boosting CO_2 photoreduction, J. Am. Chem. Soc. 2024, **146**, 3241-3249.

[36] Z. L. Liu, W. Z. Gao, L. Z. Liu, Y. X. Gao, C. Zhang, L. Chen, F. Lv, J. F. Xi, T. Du, L. P. Luo, J. C. Zhuo, W. T. Zhang, Y. W. Ji, Y. Z. Shen, W. Liu, J. L. Wang, M. C. Luo, S. J. Guo, Spin polarization induced by atomic strain of MBene promotes the $\cdot O_2^-$ production for groundwater disinfection, Nat. Commun. 2025, **16**, 197.

[37] Y. P. Long, X. Zhu, C. Gao, W. Z. Si, J. H. Li, Y. Peng, Modulation of Co spin state at Co_3O_4 crystalline-amorphous interfaces for CO oxidation and N_2O decomposition, Nat. Commun. 2025, **16**, 1048.

[38] Z. Y. Li, R. Feng, S. S. Huang, W. Li, X. H. Bu, Reconfigured spin-flip process enables efficient and persistent triplet excitons in organic-inorganic metal halides, J. Am. Chem. Soc. 2025, **147**, 7017-7027.

[39] Y. Y. Long, S. W. Zhao, L. L. Wang, H. Deng, T. Sun, J. W. Jiang, T. T. Liu, S. D. Sun, A. R. Chen, H. Zhang, Regulating high electron spin state in Co_3S_4 for enhanced water splitting, ACS Catal. 2025, **15**, 9845-9855.

[40] S. J. Kim, Y. I. Kim, B. Lamichhane, Y. H. Kim, Y. Lee, C. R. Cho, M. Cheon, J. C. Kim, H. Y. Jeong, T. Ha, J. Kim, Y. H. Lee, S. G. Kim, Y. M. Kim, S. Y. Jeong, Flat-surface-assisted and self-regulated oxidation resistance of Cu(111), Nature, 2022, **603**, 434-438.

[41] L. Lin, Y. M. Xu, Y. T. Han, R. K. Xu, T. Y. Wang, Z. M. Sun, Z. H. Yan, Spin-magnetic effect of d-π conjugation polymer enhanced O-H cleavage in water oxidation, J. Am. Chem. Soc. 2024, **146**, 7363-7372.

[42] C. Su, H. T. Cui, W. W. Wang, Y. Liu, Z. Y. Cheng, C. Wang, M. Q. Yang, L. W. Qu, Y. Li, Y. J. Cai, S. Y. He, J. X. Zheng, P. P. Zhao, P. Xu, J. B. Dai, H. Z. Tang, Bioremediation of

complex organic pollutants by engineered *Vibrio natriegens*, Nature, 2025, **642**, 1024-1033.
[43] T. Liu, S. Xiao, N. Li, J. Chen, X. Zhou, Y. Qian, C. H. Huang, Y. Zhang, Water decontamination via nonradical process by nanoconfined Fenton-like catalysts, Nat. Commun., 2023, **14**, 2881.
[44] W. Lu, N. Chen, C. P. Feng, I. Sirés, N. An, H. T. Mu, Exploring the viability of peracetic acid-mediated antibiotic degradation in wastewater through activation with electrogenerated HClO, Water Res. 2024, **261**, 122007.
[45] J. Zhou, J. Zhou, Z. Wan, Q. Qian, H. Ren, X. Yan, B. Zhou, A. Zhang, X. Pan, W. Fang, Y. Ping, Z. Sofer, Y. Huang, X. Duan, A cation-exchange approach to tunable magnetic intercalation superlattices, Nature, 2025, **643**, 683-690.
[46] X. T. Wang, T. Ouyang, L. Wang, J. H. Zhong, T. Y. Ma, Z. Q. Liu, Redox-inert Fe^{3+} ions in octahedral sites of Co-Fe spinel oxides with enhanced oxygen catalytic activity for rechargeable Zinc-air batteries, Angew. Chem. Int. Ed. 2019, **58**, 13291-13296.
[47] L. Yang, H. Cheng, H. Li, G. Sun, S. Liu, T. Ma, L. Zhang, Atomic confinement empowered CoZn dual-single-atom nanotubes for H_2O_2 production in sequential dual-cathode electro-Fenton process, Adv. Mater. 2024, **36**, 2406957.

Acknowledgements

The authors sincerely thank the financial support of the National Natural Science Foundation of China (Nos. 22306201 to Y.Q. Z and 22306202 to S.J. Z.), the Natural Science Foundation of Jiangsu Province (No. BK20231026 to Y.Q. Z.), the Young Scientific and Technological Talents Support Project of Jiangsu Association for Science and Technology (No. JSTJ-2024-414) to S.J. Z. We sincerely thank the BL14W1 beamline of Shanghai Synchrotron Radiation Facility (SSRF) for characterizations of catalysts. We sincerely thank Prof. Kai Liu's research group at Westlake University for their assistance in providing control samples to address the reviewer's comment.

Author Contributions Statement

S.J. Z. and Y.Q. Z. designed the experiment. Y.Q. Z. and X.N. Z. conducted the experiment and analyzed the results. S.H. Q. and H. L. contributed to conducting TEM, in–situ Raman characterization. S.H. Q. and Y.M. M. carried out the DFT calculation. Y. D., W. M. and M.H. Z. provided constructive suggestions for the project. S.J. Z. proposed and supervised the project. Y.Q. Z. wrote and revised the paper.

Competing Interests Statement

The authors declare no known competing interests in this work.

Figure Legends

Figure 1. Physical morphology characterizations of catalysts to verify the strained Co(111) lattice plane. (a) Schematical illustration of the local structure in CNT/Co_n. (b) HR–TEM image of CNT/Co_n. (c) AC–HADDF–STEM image of CNT/Co_n to identify the nanoparticulate Co and its exposed surface of Co(111). (d) Strain mapping images based on the GPA from its AC–HADDF–STEM characterizations in Fig. 1c. (e) Experimental and fitting FT–EXAFS curves of CNT/Co_n series. Pronounced Co–Co scattering path and weak Co–N scattering paths can be fitted. (f) XRD patterns and corresponding Rietveld refinement profiles of CNT/Co_n series. Two-theta angle at roughly ~26.4° is indexed to the carbon (002) plane. The circle means the raw data and the line represents the calculated value and the coarse underline is the difference between the raw data and the calculated value. (g) Intensity profiles of Co(111) spacing from the inverse fast Fourier transformation images in corresponding Fig. 1c and Fig. S9. (h) Co K–edge XANES of CNT/Co_n series. (i) Schematical illustrations of Co(111) lattice strain. The profiles in Figs. 1f and g from top to bottom are N–C/Co_{n-2}, CNT/Co_{n-1}, CNT/Co_n and CNT/Co_{n+1}, respectively. The elements in Fig. 1i are being adapted from the literature Y. Q. Zhang, M. H. Chen, X. Y. He, E. Z. Zhao, H. Liang, J. G. Shang, K. Liu, J. Q. Chen, S. J. Zuo, M. H. Zhou, Intrinsic strain of defect sites steering chlorination reaction for water purification, Nat. Commun. 2025, **16**, 2652. The license it was published under (CC BY-NC-ND 4.0 Attribution-NonCommercial-NoDerivatives 4.0 International https://creativecommons.org/licenses/by-nc-nd/4.0/).

Figure 2. PAA utilization by CNT/Co_n series and the possible mechanistic studies on its activation. (a) Time profile of PAA utilization via different catalysts. C means the concentration of PAA at intermediate reaction time and C_0 is the initial concentration of PAA. Reaction conditions: 10 mg L^{-1} catalysts, 200 μM PAA, 7.0±0.2 pH and room temperature. The error bars mean the standard deviation of measured values obtained by two independent experiments. (b) EPR technique using DMPO as a spin trapper for detection of reactive species from the systems of CNT/Co_n series activating PAA. (c) Exposures and types of reactive species in the systems of CNT/Co_n series activating PAA. (d) In–situ Raman spectra to capture the signal of functional group stretching during PAA activation by CNT/Co_n and CNT/Co_{n-1}. (e) Analysis of relationship among the effective magnetic moment (μ_{eff}) and ratio of high–spin electrons in CNT/Co_n series and PAA activation rate (k_{PAA}) by these catalysts. (f) Temperature–dependent EPR spectra of CNT/Co_n. (g) PAA utilization with and without 240 mT MF in 10–minute reaction. (h) Three–dimensional map

of amperometric current–time curves of CNT/Co_n in a three–electrode electrochemical system. PAA and SMX were added into the electrolyte at times of approximately 200 s and 400 s, respectively. (i) Time course of multi–potential steps for CNT/Co_n with and without 240 mT MF. Potential is referred to versus saturated calomel electrode.

Figure 3. Unveiling the strain–induced spin regulation and identifying the precise sites of Co(111) for PAA utilization. (a) Temperature–dependent magnetic susceptibility of CNT/Co series and using Curie–Weiss law to analyze the effective magnetic moment (μ_{eff}). (b) Projected DOS of Co(111) and 7%–strained Co(111). (c) Schematical geometry configuration of *d* electronic states in Co(111) and 7%–strained Co(111). (d) Strain–induced chemically structural analysis from unstrained Co(111) to 7%–strained Co(111), the analysis including *d* state magnetic moment, work function and *d*–band center based on Fermi level (d–E_f). Schematical diagrams of (e) charge density difference (CDD) and (f) spin density images from the processes of PAA interacted with the active sites. The models from top to bottom are Co(111)–step A sites, Co(111)–terrace sites and Co(111)–step B sites respectively. The three sites were 7%–strained tensile strength. Isosurface levels of the cloud in CDD plots and spin density plots are both set at 0.0015 e^{-1} $bohr^{-3}$. The bright yellow in CDD plots means the charge accumulation. The dark purple represents the spin–up density. (g) Relative energy during the processes of the three sites activating PAA molecules. The insets are schematical diagrams of the most thermodynamically favorable activating PAA process by step A sites. The atoms with red, gray, orange and albescent respectively represent the cobalt, carbon, oxygen and hydrogen.

Figure 4. PAA utilization into water decontamination. (a) Time courses of SMX degradation in catalysts activating PAA systems. C means the concentration of SMX at intermediate reaction time and C_0 is the initial concentration of SMX. Reaction conditions: 100 mg L^{-1} catalysts, 120 μM PAA, 2.5 mg L^{-1} SMX, 240 mT MF, 7.0±0.2 pH and room temperature. (b) Time courses of SMX degradation in CNT/Co_n and CNT/Co_{SA} activating PAA systems with MF ranging from 0 to 500 mT. The blue shaded areas of upper and nether respectively represent the CNT/Co_{SA}/PAA and CNT/Co_n/PAA system. (c) Scavenger experiments in SMX degradation via CNT/Co_{SA} activating PAA system for verification of active sites and reactive species by ethylenediaminetetraacetic acid disodium salt (EDTA–2Na) and TEMPO, respectively. The error bars from figures a, b and c mean the standard deviation of measured values obtained by two independent experiments. (d) Schematical illustration of bench–made continuous–flow reactor. The elements in this figure are adapted from the literature Y. Q. Zhang, M. H. Chen, X. Y. He, E. Z. Zhao, H. Liang, J. G. Shang, K. Liu, J. Q. Chen, S. J. Zuo, M. H. Zhou, Intrinsic strain of defect sites steering chlorination reaction for water purification, Nat. Commun. 2025, **16**, 2652. The license it was published under (CC BY-NC-ND 4.0 Attribution-NonCommercial-NoDerivatives 4.0 International https://creativecommons.org/licenses/by-nc-nd/4.0/). (e) The SEM image of CNT/Co_n membrane and its zoom–in image. (f) The SEM image of the cross–sectional CNT/Co_n membrane. (g) Removal performance of organics in the continuous–flow reactor. Reaction conditions: 4.0 mM PAA, 2.5 mg L^{-1} SMX or tetracycline, 5 mg L^{-1} methylene blue, 4 mL min^{-1} flow rate and 140 mT

MF. Degradation pathway of SMX in our system, mainly involving (h) hydroxylation (pathway I), (i) cleavage of S–N bond (pathway II) and (j) polymerization (pathway III).

Editorial Summary

The ferromagnetic cobalt-based catalyst with fully exposed strained Co(111) lattice plane boosts peracetic acid utilization under a mild magnetic field, producing plenty of reactive species for pollutant abatement and greener water remediations.

Peer review information: *Nature Communications* thanks Hui Huang, Minghao Sui and the other, anonymous, reviewer(s) for their contribution to the peer review of this work. A peer review file is available.

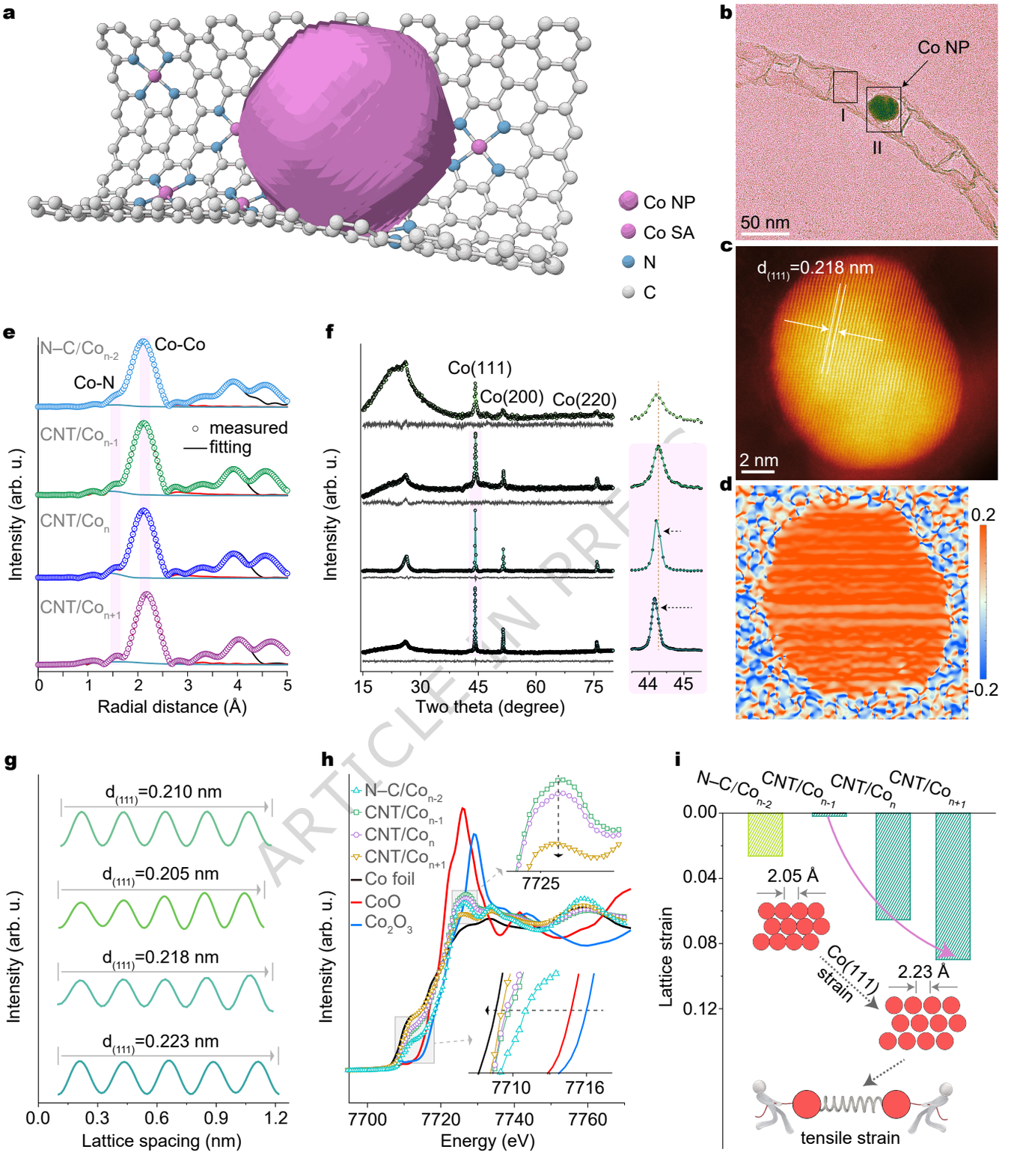
a
Co NP
Co SA
N
C
b
Co NP
I
II
50 nm
c
d(111)=0.218 nm
2 nm
d
0.2
-0.2
e
N–C/Co n-2
Co-Co
Co-N
CNT/Co n-1
measured
fitting
CNT/Co n
CNT/Co n+1
Intensity (arb. u.)
0 1 2 3 4 5
Radial distance (Å)
f
Co(111)
Co(200)
Co(220)
Intensity (arb. u.)
15 30 45 60 75
Two theta (degree)
44 45
g
d(111)=0.210 nm
d(111)=0.205 nm
d(111)=0.218 nm
d(111)=0.223 nm
Intensity (arb. u.)
0.0 0.3 0.6 0.9 1.2
Lattice spacing (nm)
h
N–C/Co n-2
CNT/Co n-1
CNT/Co n
CNT/Co n+1
Co foil
CoO
Co2O3
7725
7710 7716
Intensity (arb. u.)
7700 7720 7740 7760
Energy (eV)
i
N–C/Co n-2
CNT/Co n-1
CNT/Co n
CNT/Co n+1
0.00
0.04
0.08
0.12
Lattice strain
2.05 Å
Co(111) strain
2.23 Å
tensile strain

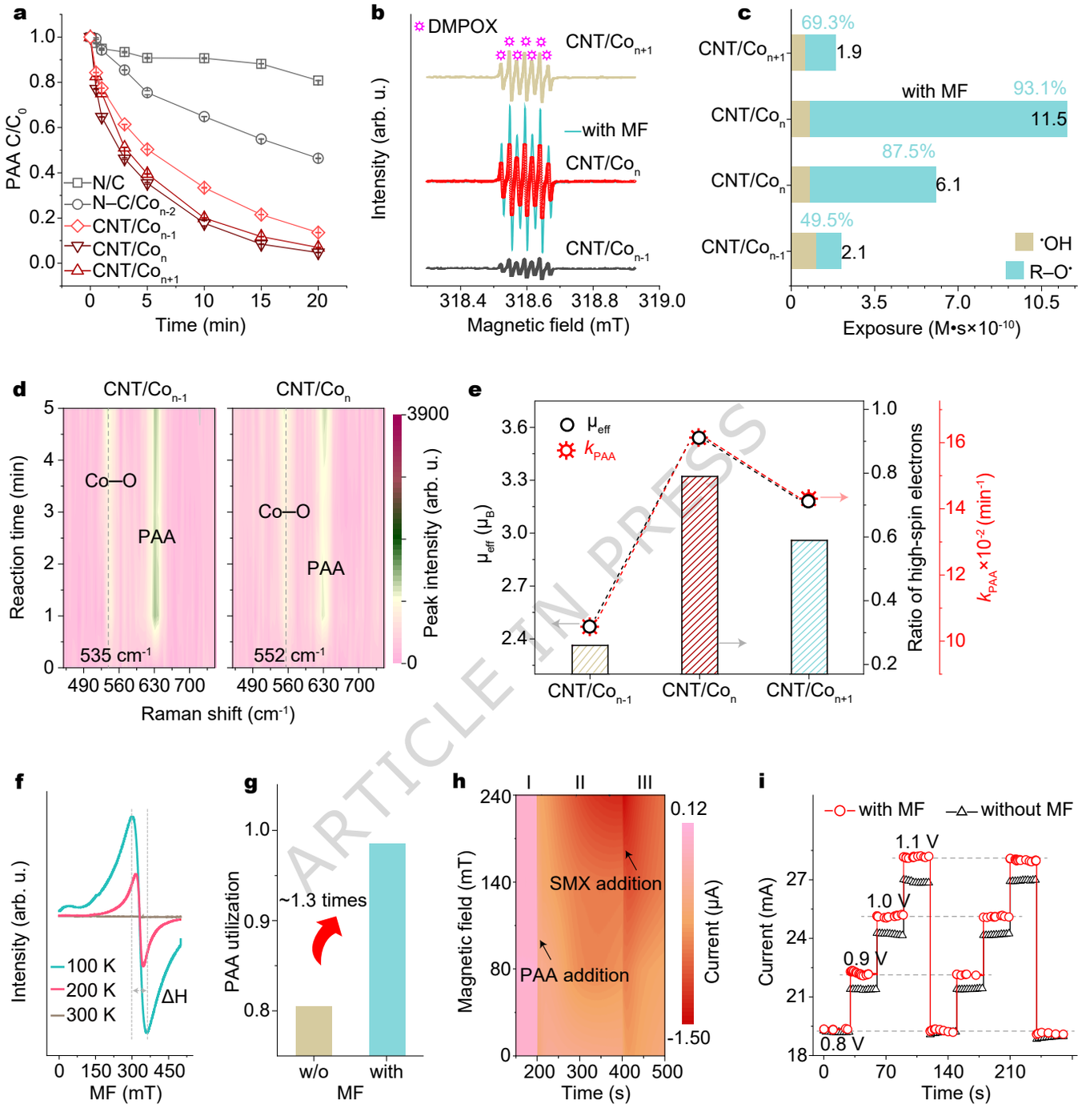

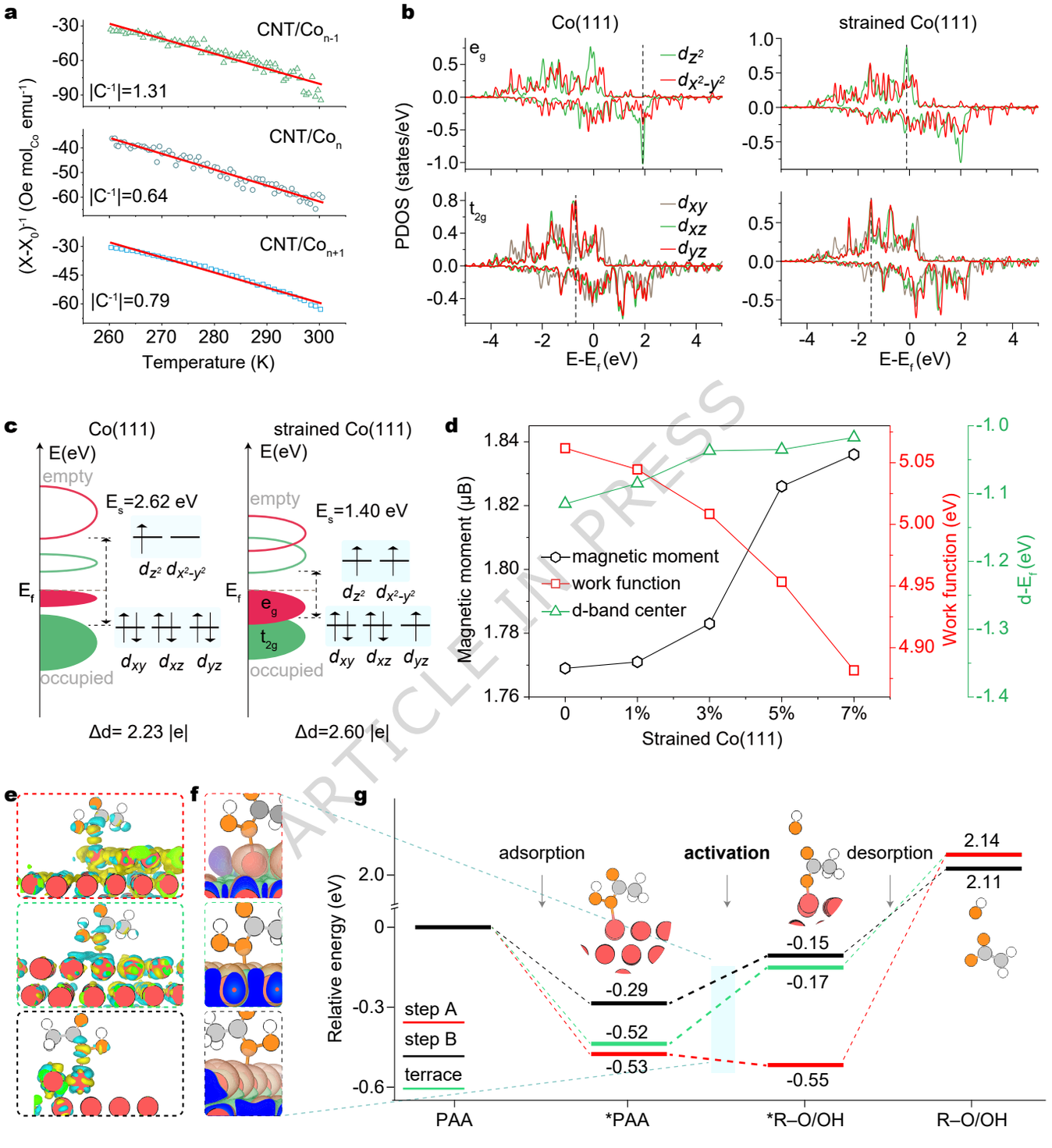

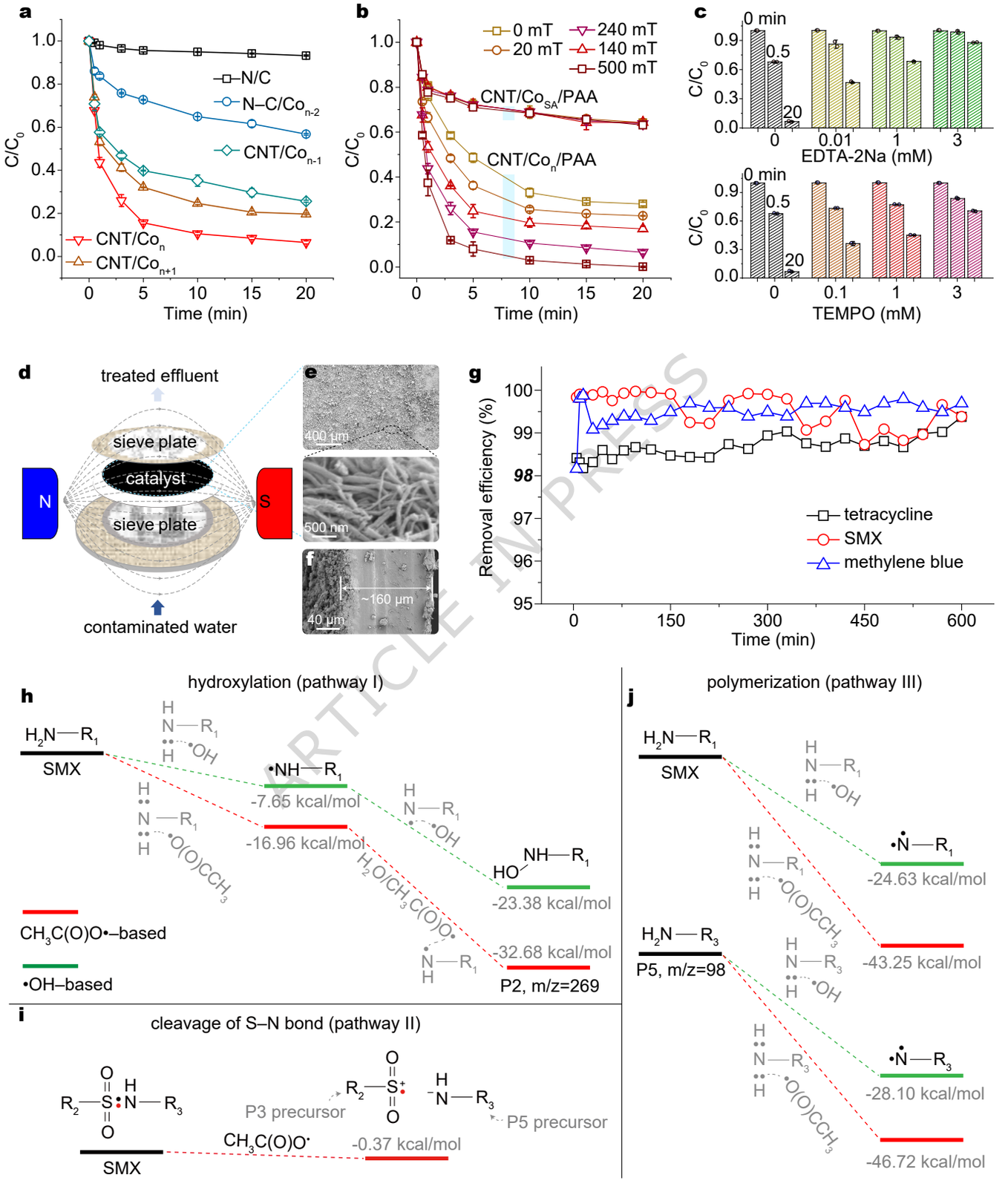
a
C/C0
Time (min)
N/C
N–C/Con-2
CNT/Con-1
CNT/Con
CNT/Con+1
b
0 mT
20 mT
240 mT
140 mT
500 mT
CNT/CoSA/PAA
CNT/Con/PAA
c
0 min
0.5
20
EDTA-2Na (mM)
TEMPO (mM)
d
treated effluent
sieve plate
catalyst
sieve plate
N
S
contaminated water
e
400 μm
500 nm
f
~160 μm
40 μm
g
Removal efficiency (%)
Time (min)
tetracycline
SMX
methylene blue
h
hydroxylation (pathway I)
SMX
-7.65 kcal/mol
-16.96 kcal/mol
-23.38 kcal/mol
-32.68 kcal/mol
P2, m/z=269
CH3C(O)O•–based
•OH–based
i
cleavage of S–N bond (pathway II)
P3 precursor
P5 precursor
SMX
-0.37 kcal/mol
j
polymerization (pathway III)
SMX
-24.63 kcal/mol
-43.25 kcal/mol
P5, m/z=98
-28.10 kcal/mol
-46.72 kcal/mol